



Analysis of gravity disturbance for boundary structures in the Aegean Sea and Western Anatolia

Fikret Doğru^{1,3} and Oya Pamukçu²

¹Department of Geophysical Engineering, Oltu Earth Sciences Faculty, Ataturk University, Oltu, Erzurum, Turkey

²Geophysical Engineering, Engineering Faculty, Dokuz Eylul University, Buca, İzmir, Turkey

³The Institute of Natural and Applied Sciences, Dokuz Eylul University, İzmir, Turkey

Received 24 October 2018, in final form 17 May 2019

Western Anatolia has been shaped N–S-trending extensional tectonic regime and W–E trending horst, grabens and active faults due to the collision of Africa, Arabian and Eurasia plates. The borders of the Aegean Sea tectonic is limited between eastern of Greece, western of Anatolia and Hellenic subduction zone in the south of Crete. To evaluate these tectonic elements gravity disturbance data of the Aegean Sea and Western Anatolia was used in this study. It is thought that the gravity disturbance data reflects the tectonic elements and discontinuities way better than gravity anomaly due to the calculation from the difference between gravity and normal gravity at the same point so thus the tensors and invariants of the study area were calculated and the power spectrum method was applied to the gravity disturbance data. Various boundary analysis methods were applied to the gravity disturbance data to compare the discontinuities obtained from the tensors both theoretical and case study. These methods were tested initially on theoretical data. Within the scope of the theoretical study, a single model and three bodies model were taken into consideration. When the results are examined, it is observed that the T_{zz} tensor component gives very clear information about the location of the structure. Likewise, when the T_{xx} , T_{yy} components and invariant results are examined, the vertical and horizontal boundaries were successfully obtained. In addition, the mean depths of these structures were determined using the power spectrum method. In the case application stage, the gravity disturbance data obtained from the Earth Gravitational Model of the eastern of the Aegean Sea and western of Anatolia were evaluated. The tensor and invariants of this gravity disturbance data were first calculated. New possible discontinuities have been identified in the tensors and some of the obtained discontinuities were clarified in their previous discussions. Also, the mean depths of the possible structures were calculated by the power spectrum method at four profiles taken from gravity disturbance data. These depth values are consistent with the depth values of the structural discontinuities obtained from previous studies. Finally, the upward continuation was applied to T_{yy} , T_{yz} and T_{zz} tensors up to 20 km. The positive anomaly values in T_{yz} and

T_{zz} components and negative anomaly values in T_{yy} component are consistent with the Western Anatolia Transfer Zone. The structural differences between the eastern and the western of Western Anatolia are noteworthy in the upward continued results of the tensors. In addition, the positive and negative anomalies are notable in areas where the big earthquakes occurred in the last 3 years in the T_{yz} invariants.

Keywords: gravity disturbance, the Aegean Sea, Western of Anatolia, tensor, invariant

1. Introduction

Western Anatolia is one of the most active regions in point of continental expansion and has high seismic activity on a continental scale. Different views have been raised about the evolution of the Western Anatolia expansion system. One of these views, the tectonic escape model states that the Anatolian Plate moved west along the Eastern Anatolian and North Anatolian faults that developed as a result of the collision of the Arabic and Eurasian plates. Thus, the W-SW directional tectonic escape of the Anatolian plate formed the extensional tectonics regime which caused the development of the horst-graben system in Western Anatolia (Dewey and Şengör, 1979; Şengör, 1979, 1987; Şengör et al., 1985). According to LePichon and Angelier (1979) and Meulenkaamp et al. (1988), in the arc expansion model, the S-SW directional migration of the Hellenic Trench system caused arc expansion and the formation of the horst-graben system. Another proposed view, the orogenic collapse is related to the dilation and expansion of the crust (Dewey, 1988; Seyitoğlu and Scott, 1991). In the McKenzie model, the plate model is given in two stages for Western Anatolia. In the first stage; according to Africa, the Arabic Plate that moves faster towards Eurasia is overlaid on the Anatolian Plate. This over thrust causes the Anatolian Plate to be pushed westward along the North and East Anatolian Faults. In the second stage, this proposal was further improved and interpreted. The continental lithosphere of Western Anatolia stretched along with a number of E-W directional faults in this area (McKenzie, 1972). Lastly, Alptekin (1973) suggested that the westward movement of the Turkey-Aegean plate is the result of convective currents in the mantle and the effects of thermal sources in Eastern Anatolia (Fig. 1).

Gravity disturbing tensors are the second derivatives of the Earth's gravitational disturbing potential in the local North-oriented reference frame (Bucha and Janák, 2013). Also, the invariants of disturbing tensors are composed of disturbing tensors (Pedersen and Rasmussen, 1990). Gravity gradient tensor and invariants have been used for determining discontinuities and locating subsurface structures for three decades. Pedersen and Rasmussen (1990) used the gradient tensor of potential field anomalies to show strategies of data collection and processing. Zhang et al. (2000) used Euler convolution of gravity tensor gradient data for determining the depth and location of subsurface bodies. Zhdanov et al. (2004) applied inversion on gravity gradient tensor to obtain geo-



Figure 1. General tectonic map of the region (modified from Makris and Stobbe, 1984; McClusky et al., 2000; Bozkurt, 2001; Gönenç and Akgün, 2012) (question marks indicate discussed and newly proposed faults, white stars represent the big earthquakes that occurred in the last three years).

logical targets boundary sharply. Routh et al. (2001) used gravity and tensor gravity data for the imaging base of the salt. Murphy and Brewster (2007) used gravity gradiometry for detecting salt body geometries imaging over offshore Norway. Dransfield and Milkereit (2007) used gravity gradients for searching mineral deposits. Klokočník et al. (2014) used gravity disturbances and invariants with suggestions of geomorphological and geodynamic interpretations for further studies. Mataragio and Kieley (2009) used gradient invariants for detection sulfide mineralization area. Dickinson et al. (2009) used gravity tensor and invariants for a project of hydrocarbon and mineral exploration. Murphy and Dickinson (2010) used full tensor gravity data for geological mapping and locating geological boundaries. Beiki and Pedersen (2010) used gravity gradient tensor for locating geological bodies. Oruc (2010) used gravity tensor and vertical components to detect the depth of the subsurface bodies. Oruc et al. (2013) used gravity gradient tensors for structural interpretation of Erzurum Basin. Zuo and Hu (2015) used gravity gradient tensors to detect the edges of geological bodies. Zhou (2016) used a ratio of gravity and full tensor gradient invariants for depth estimation. Zuo et al. (2017) used gravity gradients for determining the position of complex subsurface geological structures.

Large magnitude earthquakes occurred in the Western Anatolian and the Aegean Sea transition region where includes important tectonic elements. In

this context, the boundaries and depths of the known structures were determined and the satellite gravity data were used to determine the sources of this activity in the region. The satellite gravitational, terrestrial gravity and GPS/GNSS data were successfully used to clarify tectonic elements in the Western Anatolian by previous studies (Çırmık et al., 2017; Çırmık and Pamukçu, 2017; Doğru et al., 2018; Kahveci et al., 2019; Malaliçi et al., 2019). The applications of boundary analysis, power spectrum, tensor and invariant methods were applied on theoretical data in order to determine the extension of a 3-D structure in this study. In the second stage, the same methods were applied to case study data in Western Anatolia and the Aegean Sea transition zone where has the high seismic activity. Satellite gravity data were firstly applied to define discontinuities and determine previously unknown discontinuities.

In this stage, firstly, the theoretical models obtained from only a sphere body and three bodies (sphere, horizontal and vertical cylinders) were used to show the effectiveness of the boundary analysis, power spectrum, tensor and invariant methods. 3-D distribution of the structures within the theoretical stage was interpreted successfully so that the success of the application method was tested successfully. Then, the same methods were applied to the gravitational disturbing potential of Earth Gravitational Model 2008 (EGM2008) (Pavlis et al., 2008) data. After that, EGM2008 data was used to obtain tensor components. The invariants were calculated from gravity disturbing tensor components. The locations of active faults were obtained compatible with high low anomaly boundary in the tensor anomalies, especially in T_{zz} . In addition, the power spectrum method was applied on profiles which are taken from both theoretical and case data. The depths were obtained successfully in theoretical study and the depths of shallow structures were obtained close to the known values from previous studies. In addition, the new discontinuity obtained as a zone in this study for the first time in the southwest is particularly noticeable in the Bouguer gravity disturbance and T_{zz} tensor component.

2. Methods

2.1. Gravity disturbance and disturbing tensors in the local North-oriented reference frame

The gravity disturbance is calculated via the following formula (Bucha and Janák, 2013):

$$-\frac{\partial T(r, \varphi, \lambda)}{\partial r} = \frac{GM}{r^2} \sum_{n=n_{\min}}^{n_{\max}} \left(\frac{R}{r}\right)^n (n+1) \sum_{m=0}^n (\Delta \bar{C}_{n,m} \cos m\lambda + \Delta \bar{S}_{n,m} \sin m\lambda) \bar{P}_{n,m}(\sin \varphi) \quad (1)$$

$$T(r, \varphi, \lambda) = \begin{pmatrix} T_{xx} & T_{xy} & T_{xz} \\ T_{yx} & T_{yy} & T_{yz} \\ T_{zx} & T_{zy} & T_{zz} \end{pmatrix} \quad (2)$$

$$T(r, \varphi, \lambda) = \frac{GM}{r^3} \sum_{n=n_{\min}}^{n_{\max}} \left(\frac{R}{r}\right)^n \sum_{m=-n}^n \Delta \bar{C}_{n,m} Q_m(\lambda) (a_{n,m} \bar{P}_{n,|m|-2}(\sin \varphi) + [b_{n,m} - (n+1)(n+2)] \bar{P}_{n,|m|}(\sin \varphi) + c_{n,m} \bar{P}_{n,|m|+2}(\sin \varphi)) \quad (3)$$

$$T_{xy}(r, \varphi, \lambda) = \frac{GM}{r^3} \sum_{n=0}^{n_{\max}} \left(\frac{R}{r}\right)^n \sum_{m=-n}^n \Delta \bar{C}_{n,m} Q_{-m}(\lambda) (d_{n,m} \bar{P}_{n-1,|m|-2}(\sin \varphi) + g_{n,m} \bar{P}_{n-1,|m|}(\sin \varphi) + h_{n,m} \bar{P}_{n-1,|m|+2}(\sin \varphi)), m \neq 0 \quad (4)$$

$$T_{xz}(r, \varphi, \lambda) = \frac{GM}{r^3} \sum_{n=0}^{n_{\max}} \left(\frac{R}{r}\right)^n \sum_{m=-n}^n \Delta \bar{C}_{n,m} Q_m(\lambda) (\beta_{n,m} \bar{P}_{n,|m|-1}(\sin \varphi) + \gamma_{n,m} \bar{P}_{n,|m|+1}(\sin \varphi)) \quad (5)$$

$$T_{yy}(r, \varphi, \lambda) = -\frac{GM}{r^3} \sum_{n=n_{\min}}^{n_{\max}} \left(\frac{R}{r}\right)^n \sum_{m=-n}^n \Delta \bar{C}_{n,m} Q_m(\lambda) (a_{n,m} \bar{P}_{n,|m|-2}(\sin \varphi) + b_{n,m} \bar{P}_{n,|m|}(\sin \varphi) + c_{n,m} \bar{P}_{n,|m|+2}(\sin \varphi)) \quad (6)$$

$$T_{yz}(r, \varphi, \lambda) = -\frac{GM}{r^3} \sum_{n=0}^{n_{\max}} \left(\frac{R}{r}\right)^n \sum_{m=-n}^n \Delta \bar{C}_{n,m} Q_{-m}(\lambda) (\mu_{n,m} \bar{P}_{n-1,|m|-1}(\sin \varphi) + \nu_{n,m} \bar{P}_{n-1,|m|+1}(\sin \varphi)), m \neq 0 \quad (7)$$

$$T_{zz}(r, \varphi, \lambda) = -\frac{GM}{r^3} \sum_{n=n_{\min}}^{n_{\max}} \left(\frac{R}{r}\right)^n (n+1)(n+2) \sum_{m=-n}^n \Delta \bar{C}_{n,m} Q_m(\lambda) \bar{P}_{n,|m|}(\sin \varphi) \quad (8)$$

where r , φ and λ are the spherical radius, latitude and longitude; n, m are spherical harmonic degree and order; n_{\min} and n_{\max} are minimum and a maximum

degree of spherical harmonic expansion; is 4 fully normalized associated Legendre function of the first kind of degree n and order m ; and are 4 fully normalized spherical harmonic coefficients of degree n and order m related to global geopotential model; is the Geocentric gravitational constant times Earth mass, and R the radius of the reference sphere. In addition, and are differences in spherical harmonic coefficients (the actual gravity field from a gravity field model minus a normal gravity field) (Bucha and Janák, 2013).

2.2. Logarithmic power spectrum method

Power spectrum analysis predicts the mean depth of the interfaces taking in consideration the log of the power of the Bouguer gravity spectrum as a function of wavenumber/frequency supposing uncorrelated distribution of subsurface structures (Spector and Grant, 1970).

The logarithmic power spectrum was used in this study. The logarithmic power spectrum shows the line segments at different slopes in a different radial wave number (kr) order. In general, the line segments corresponding to small radial wave numbers are represented by deep local sources, the medium-wave numbers are represented by shallow sources and the high-wave numbers are represented by noise in the data (Spector and Grant, 1970; Pawlowski and Hansen, 1990; Pawlowski, 1994). The mean depth of each equivalent layer is calculated from Equation 9,

$$h = \frac{B(kr_1) - B(kr_2)}{2(kr_2 - kr_1)} \quad (9)$$

where kr_1 and kr_2 are the start and end radial wave numbers of the overlaid line. $B(kr_1)$ and $B(kr_2)$ are the logarithmic power spectrum values corresponding to these wave numbers.

2.3. Invariants of gradient tensor matrix

Gravity gradient tensor $\mathbf{\Gamma}$ (the Marussi tensor) (Klokočník et al., 2014) is a tensor of the second derivatives of the disturbing potential V and is computed by means of $\Delta\bar{C}_{n,m}$ and $\Delta\bar{S}_{n,m}$ of the particular gravity field model known to the maximum degree n_{max} :

$$\mathbf{\Gamma} = \begin{bmatrix} \Gamma_{11} & \Gamma_{12} & \Gamma_{13} \\ \Gamma_{21} & \Gamma_{22} & \Gamma_{23} \\ \Gamma_{31} & \Gamma_{32} & \Gamma_{33} \end{bmatrix} = \begin{bmatrix} \frac{\partial^2 V}{\partial x^2} & \frac{\partial^2 V}{\partial x \partial y} & \frac{\partial^2 V}{\partial x \partial z} \\ \frac{\partial^2 V}{\partial x \partial y} & \frac{\partial^2 V}{\partial y^2} & \frac{\partial^2 V}{\partial y \partial z} \\ \frac{\partial^2 V}{\partial z \partial x} & \frac{\partial^2 V}{\partial z \partial y} & \frac{\partial^2 V}{\partial y^2} \end{bmatrix} = \begin{bmatrix} T_{xx} & T_{xy} & T_{xz} \\ T_{yx} & T_{yy} & T_{yz} \\ T_{zx} & T_{zy} & T_{zz} \end{bmatrix} \quad (10)$$

The tensor components Γ_{33} are used in local scales to identify and map geological contact information, edges of source targets or structural/stratigraphic contact information. The horizontal components help identify the shape and geological setting of a target body. The quantity Γ_{33} is best suited for target body detection, helps to define isopath/density relationships of a body mass with relation to its geological setting (Murphy and Dickinson, 2009).

Under any coordinate transformation, Γ preserves three invariants:

$$I_0 = \text{trace}(\Gamma) = \Gamma_{11} + \Gamma_{22} + \Gamma_{33} \quad (11)$$

$$I_1 = \Gamma_{11}\Gamma_{22} + \Gamma_{22}\Gamma_{33} + \Gamma_{33}\Gamma_{11} - \Gamma_{12}^2 - \Gamma_{23}^2 - \Gamma_{13}^2 \quad (12)$$

$$I_2 = \det(\Gamma) = \Gamma_{11}(\Gamma_{22}\Gamma_{33} - \Gamma_{23}^2) + \Gamma_{12}(\Gamma_{23}\Gamma_{13} - \Gamma_{12}\Gamma_{33}) + \Gamma_{13}(\Gamma_{12}\Gamma_{23} - \Gamma_{13}\Gamma_{22}) \quad (13)$$

2.4. Geological boundary analysis

A number of methods have been proposed to make subtle anomalies more visible. The first filter developed for this purpose was the tilt angle (Miller and Singh, 1994), which is the ratio of the vertical derivative to the absolute value of the horizontal derivative of the potential field. The tilt angle is given by:

$$\text{Tilt} = \tan^{-1} \left(\frac{\frac{\partial T}{\partial z}}{THDR} \right) \quad (14)$$

where

$$THDR = \sqrt{\left(\frac{\partial T}{\partial x}\right)^2 + \left(\frac{\partial T}{\partial y}\right)^2} \quad (15)$$

T is the potential anomaly and $THDR$ is the total horizontal derivatives (Cordell and Grauch, 1985). The tilt angle amplitudes are restricted to values between $-\pi/2$ and $+\pi/2$; thus the method delimitates the amplitude variations into a certain range. The tilt angle is like an automatic-gain-control filter and responds equally well to shallow and deep sources. The tilt angle produces a zero value over the source edges (Arisoy and Dikmen, 2013). In addition, AS is the analytic signal for the 3D case (Roest et al., 1992).

$$AS = \sqrt{\left(\frac{\partial T}{\partial x}\right)^2 + \left(\frac{\partial T}{\partial y}\right)^2 + \left(\frac{\partial T}{\partial z}\right)^2} \quad (16)$$

Theta map that is the normalization of the $THDR$ by the AS was proposed by Wijns et al. (2005).

$$\cos\theta = \frac{THDR}{AS} \quad (17)$$

3. Applications

3.1. Theoretical study

In the first stage of applications, presented methods were applied to theoretical data. For this purpose, $100 \text{ km} \times 100 \text{ km}$ area was selected for modeling sphere. The center depth of the sphere was 50 km, the radius and depth of sphere were 5 km and 10 km respectively. Density contrast was 1 g/cm^3 (Fig. 2a). The

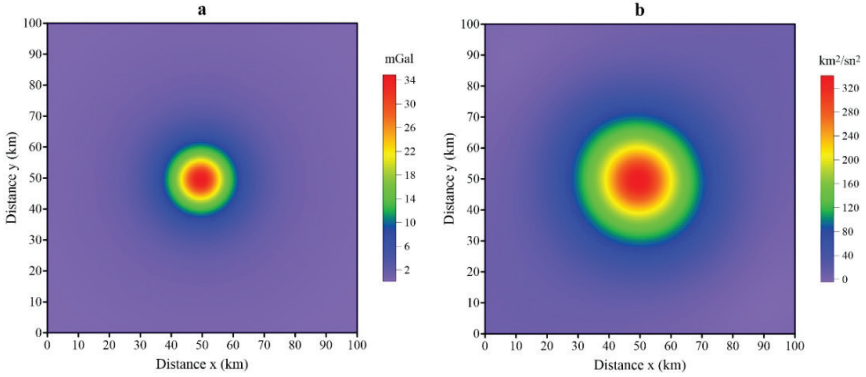


Figure 2. The theoretical gravity anomaly of the sphere and its potential: (a) the theoretical gravity anomaly and (b) potential anomaly of (a).

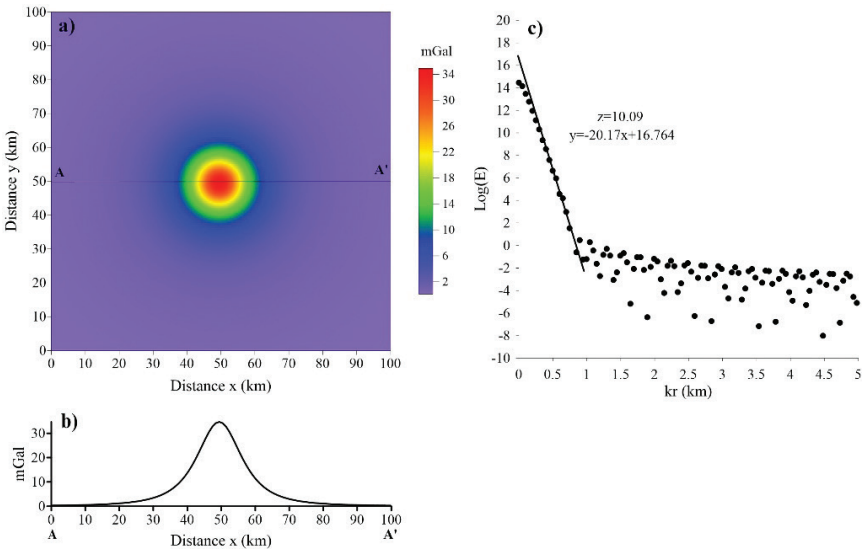


Figure 3. The theoretical gravity anomaly of the sphere, the profile of theoretical anomaly and power spectrum of the profile: (a) the theoretical gravity anomaly, (b) the anomaly of A-A' profile and (c) the power spectrum result of A-A' profile.

theoretical gravity anomaly and potential anomaly values change between 0–34 mGal and 0–320 km²/sn² respectively.

The power spectrum was applied to the A-A' profile (Fig. 3b) that was taken from theoretical gravity anomaly in Fig. 3a (Fig. 3c). The depth was obtained as 10.09 km from power spectrum and the error was obtained as % 0.9 mGal. Then, tensors of theoretical sphere anomaly were computed using potential anomaly in Fig. 2b. Negative to positive values from inside to outside of the sphere were obtained in the T_{xx} and T_{yy} components of tensors (Figs. 4a and 4d). Depending on the direction of the derivative, one side negative and other side positive values were obtained in the T_{xz} and T_{yz} components of tensors (Figs. 4c and 4e). In the T_{xy} component, the direction of increase and decrease of the x and y directional amplitude changes were observed as being the center sphere (Fig. 4b). Positive

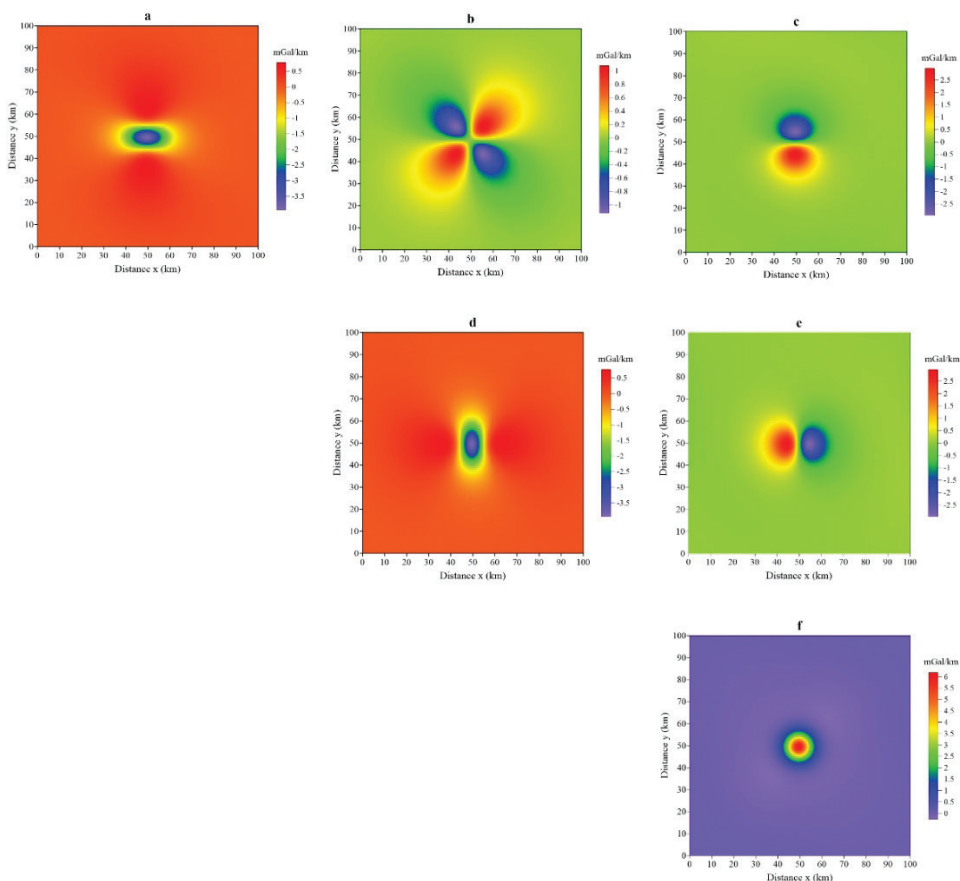


Figure 4. The tensor results of theoretical sphere anomaly: (a) T_{xx} , (b) T_{xy} , (c) T_{xz} , (d) T_{yy} , (e) T_{yz} and (f) T_{zz} .

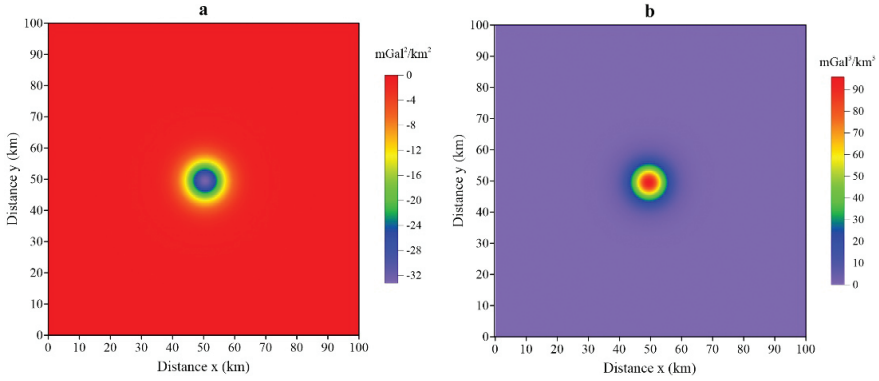


Figure 5. The results of I1 and I2 invariants: (a) the I1 invariant and (b) the I2 invariant.

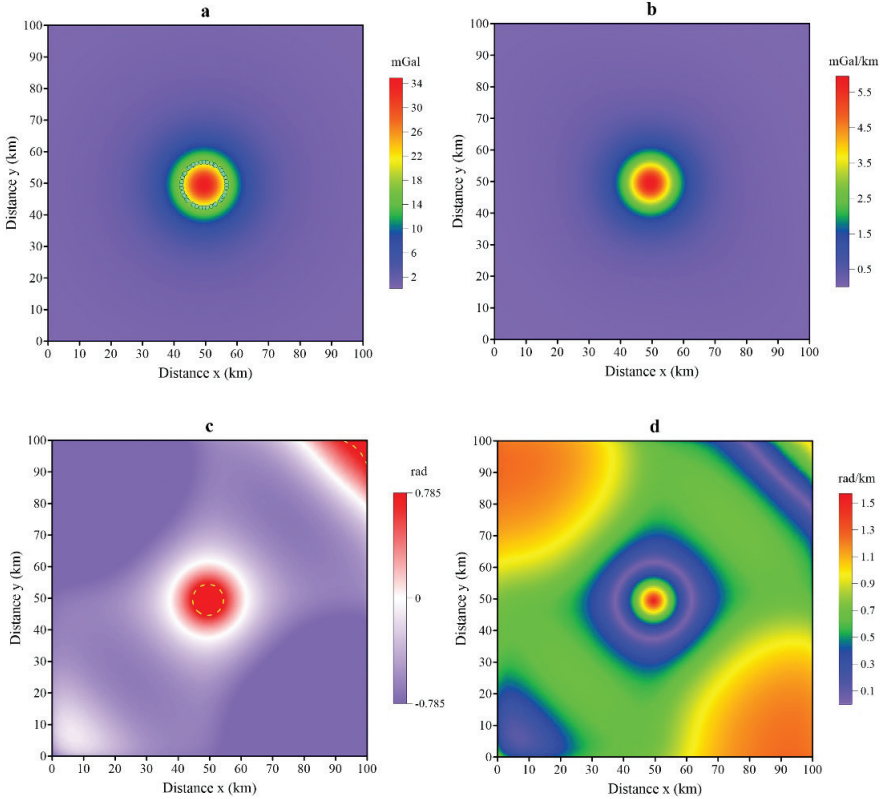


Figure 6. Boundary analysis results of theoretical sphere anomaly: (a) THDR result (Cyan dots) was overlaid on theoretical sphere anomaly, (b) the result of AS, (c) the result of tilt angle (yellow dashed line indicates $+\pi/2$ values of Tilt angle corresponding to source boundary) and (d) the result of theta map.

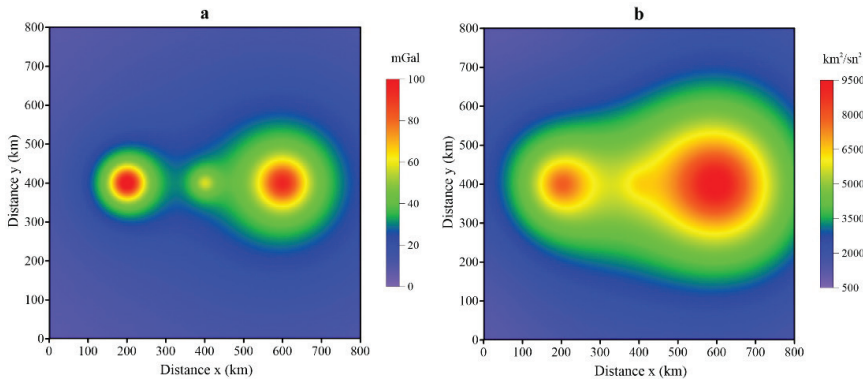


Figure 7. The theoretical total gravity anomaly of three bodies which are horizontal cylinder, sphere and vertical cylinder (in order from left to right) at 45 km, 40 km and 50 km depths respectively (radiuses are 10, 12 and 15 km, respectively) and its potential: (a) the theoretical total gravity anomaly and (b) potential anomaly of (a).

to negative values from inside to outside of the sphere were obtained in the T_{zz} component and also the shape of the body was obtained in this tensor component notably (Fig. 4f). In addition, the I1 and I2 invariants of the theoretical anomaly were computed and the location and shape of the body were recognized clearly (Figs. 5a and 5b). The values changed negative to positive from inside to outside of the subsurface structure in the I1 invariant (Fig. 5a). Also, the values

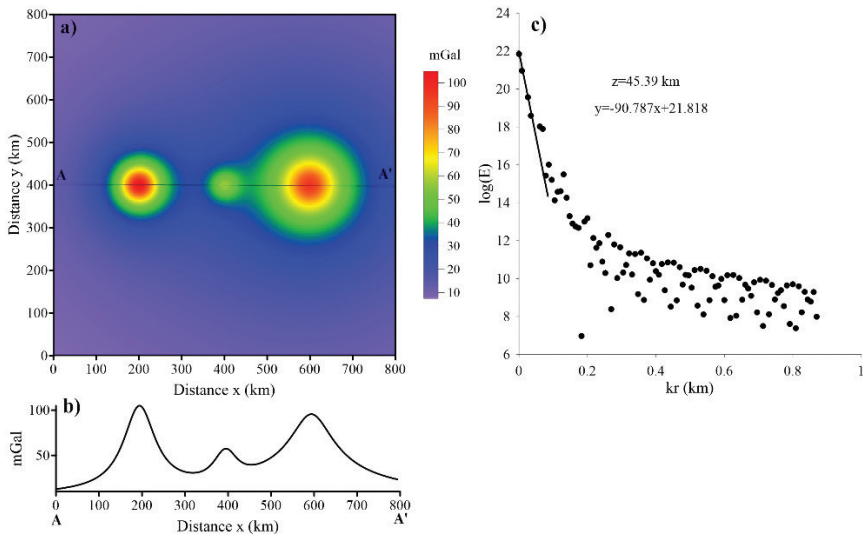


Figure 8. The theoretical total gravity anomaly of a horizontal cylinder, sphere and vertical cylinder, the profile of theoretical total anomaly and power spectrum of the profile: (a) the theoretical total gravity anomaly, (b) the anomaly of A-A' profile and (c) the power spectrum result of A-A' profile.

changed positive to negative from inside to outside of subsurface structure in the I2 invariant (Fig. 5b). In addition, the boundaries of buried structures were obtained clearly in the results of boundary analysis methods. *THDR* and *AS* results were obtained similar and the *THDR* result was overlaid on the theoretical sphere anomaly. The values changed from maximum to minimum inside to outside of the buried structure (Figs. 6a and 6b). The positive values were observed in the center of the structure and negative values were observed in the outside of the body in the Tilt angle result. $+\pi/2$ values of tilt angle corresponding to source boundary were obtained at the borders of the sphere (Fig. 6c). Also, the values changed maximum to minimum till to outside of the model borders and the values changed increase along SE-NW and increase to decrease along NE-SW in the result of Theta map (Fig. 6d).

In the second part of the theoretical study, the theoretical total gravity anomaly of three bodies which are a horizontal cylinder, a sphere and a vertical cyl-

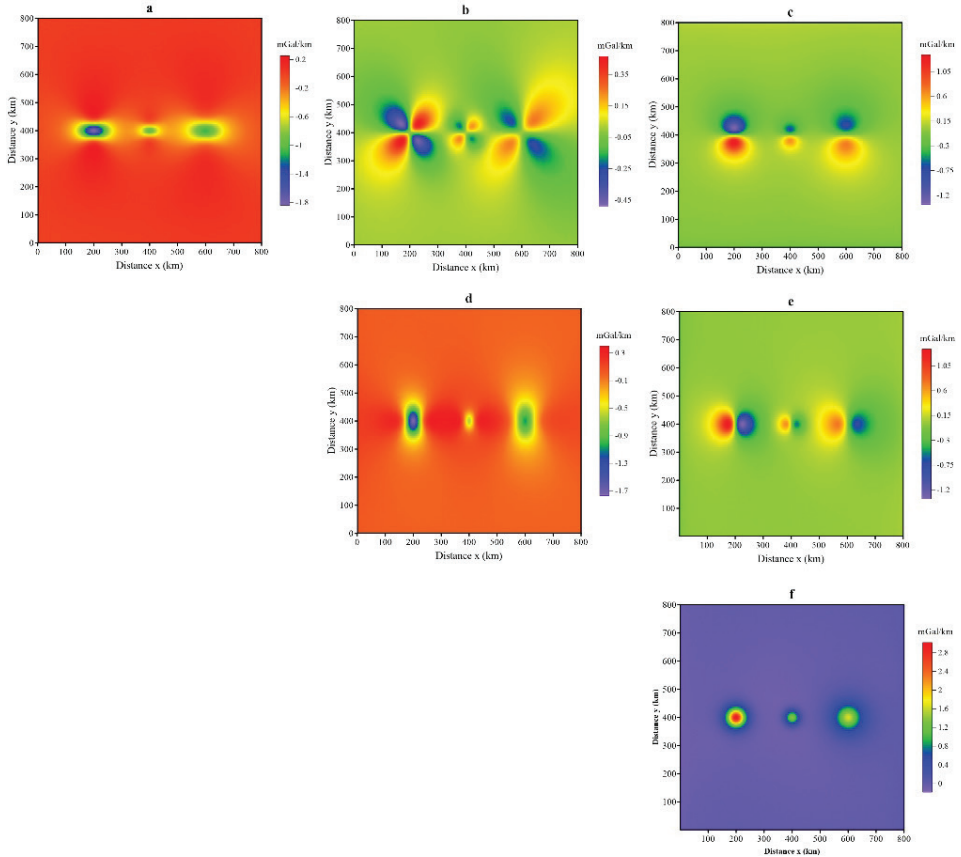


Figure 9. The tensor results of theoretical total gravity anomaly of three bodies: (a) T_{xx} , (b) T_{xy} , (c) T_{xz} , (d) T_{yy} , (e) T_{yz} and (f) T_{zz} .

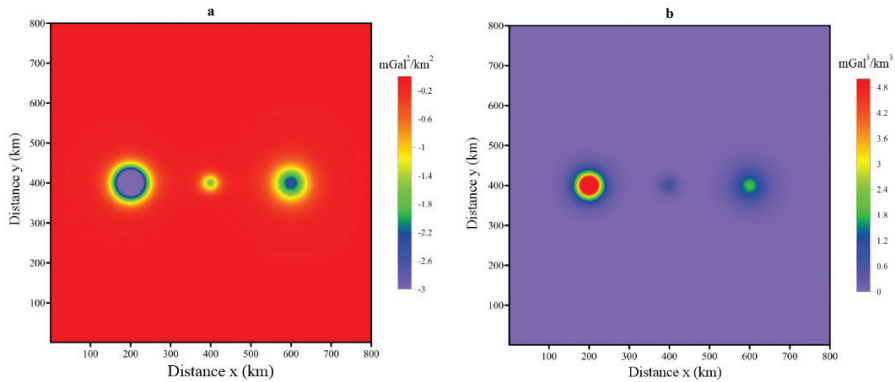


Figure 10. The results of I1 and I2 invariants: (a) the I1 invariant and (b) the I2 invariant.

inder were used to apply presented methods (Fig. 7a). The potential of theoretical total gravity anomaly was computed to calculate tensors and invariants (Fig. 7b). In the first stage, the power spectrum of profile anomaly (Fig. 8b) was computed from the theoretical total anomaly in Fig. 8a and the depth was obtained as 45.39 km with % 0.86 mGal error (Fig. 8c). It is shown that the value of horizontal cylinder anomaly was the highest and the value of sphere anomaly is the lowest so thus the boundaries of the horizontal and vertical cylinders were obtained more clearly than sphere apart from the depth and radius effect. Besides the deepest structure was a vertical cylinder, the radius of the vertical cylinder was the biggest so thus anomalies of vertical and horizontal cylinders repressed the sphere anomaly (Fig. 9). Also, it was shown that the locations of vertical and horizontal cylinders were obtained more clearly in the I1 and I2 invariants maps (Figs. 10a and 10b). In addition, boundary analysis methods were applied successfully and the locations of buried bodies are obtained as clear as the results in the T_{zz} tensor and invariants. *THDR* and *AS* results were obtained similar and the values change from maximum to minimum inside to the outside of the structure (Fig. 11a and 11b). The positive values were observed in the center of the structure and negative values were observed in the outside of the bodies in the Tilt angle result. $+\pi / 2$ values of tilt angle corresponding to source boundaries were obtained at the borders of the three bodies (Fig. 11c). Also, the borders of structures were observed easily in the result of theta map (Fig. 11d).

3.2. Case study

In the case study, gravity disturbance data of the area between 25–28° latitudes and 36.5–40.5° longitudes was calculated using GrafLAB software (Bucha and Janák, 2013). Topographic and isostatic effects have been removed using the Spherical harmonic representation of the Earth's topographic-isostatic gravitational potential (RWI_TOIS_2012_plusGRS80) (Grombein et al., 2014) to re-

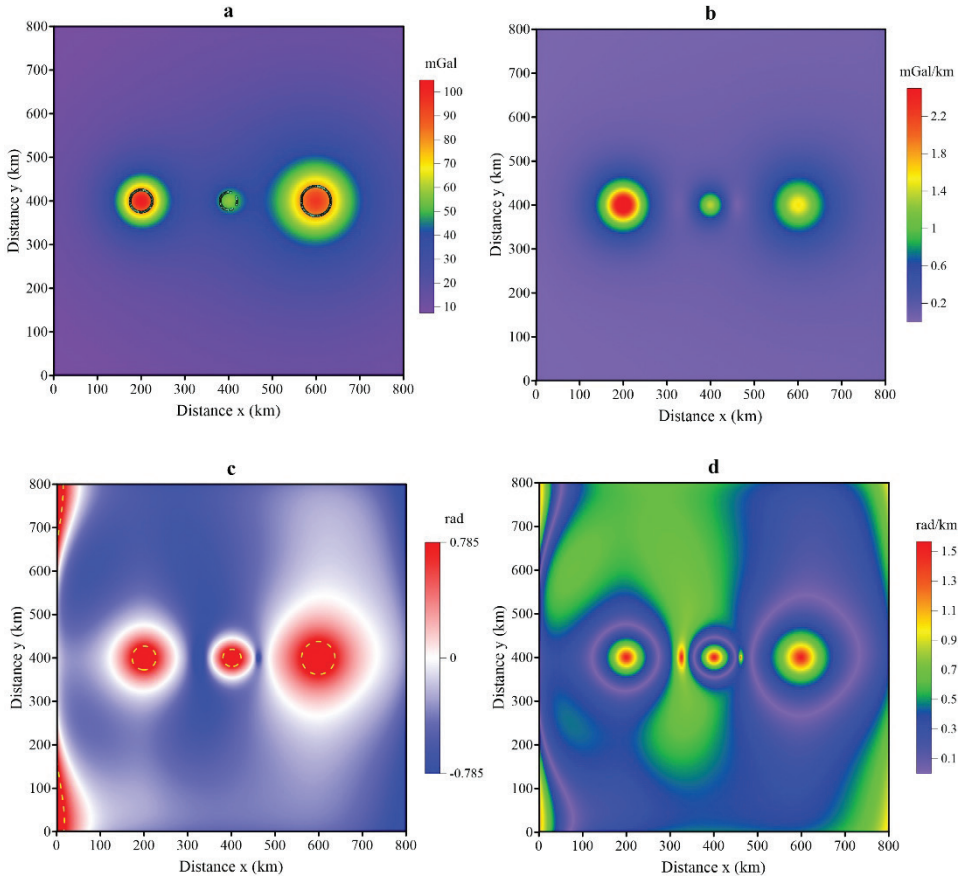


Figure 11. Boundary analysis results of theoretical total gravity anomaly of three bodies: (a) *THDR* result (Cyan dots) was overlaid on theoretical sphere anomaly, (b) the result of *AS*, (c) the result of tilt angle (yellow dashed line indicates $+\pi/2$ values of Tilt angle corresponding to source boundary) and (d) the result of theta map.

veal shallow discontinuities and structure-based effects (Fig. 12). At this stage of the study, the presented methods that were implemented on the theoretical application were applied to gravity disturbance data. First, sections were taken from the Bouguer gravity disturbances map (Fig. 12) and average depth was determined by logarithmic power spectrum method (Fig. 13). Then, the tensor analysis methods were performed to the Bouguer gravity disturbance anomaly values in Fig. 12 (Fig. 14).

In the other stage of the study, the invariants of Bouguer gravity disturbance tensors which were calculated using the values in Fig. 14 for the study area, were presented in Fig. 15 along with the earthquake focal depths and geothermal hot

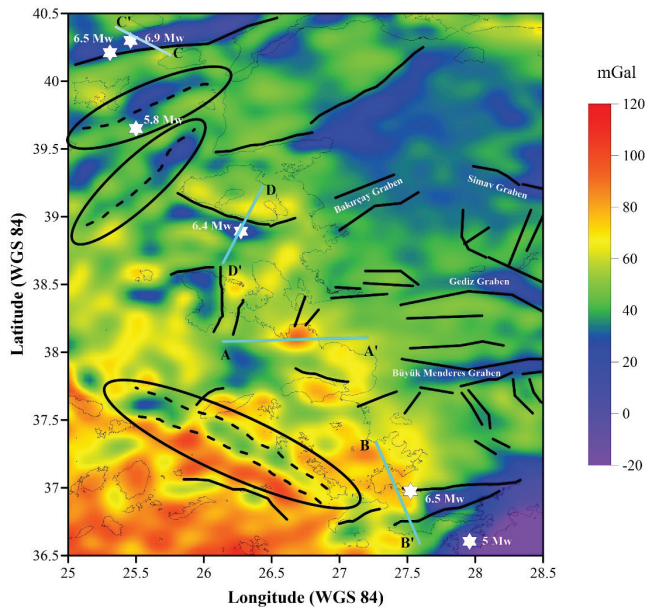


Figure 12. Bouguer gravity disturbance of the study area (solid black lines represent the active fault systems, the light black line shows the coastline, dashed lines show the possible faults and white stars represent the big earthquakes that occurred in the last three years, cyan lines shows the direction of profiles).

spots distribution at the same location. In the next step, *THDR*, *AS*, tilt angle and theta map methods were applied to the Bouguer gravity disturbances values in Fig. 12 (Fig. 16). Obtained findings were evaluated together with structural elements. Finally, in order to investigate the regional change of T_{yy} , T_{yz} and T_{zz} components, an analytical continuation method was applied to the anomaly values in Fig. 14 (Fig. 17).

4. Discussions

Firstly, in the first part of the study, the mentioned methods were applied to the theoretical data. As the theoretical model, two different models were used, the first model contains a single sphere and the second model contains the horizontal and vertical cylinders with the sphere. In the second model, the structures with different depths, radius and locations were used. Then, the potentials of the anomalies obtained from theoretical models were calculated. Obtained potential anomalies are used for tensor calculations. The locations and boundaries of the structures were determined in the results of the tensor. In addition, boundary analysis methods were applied and compared with the structure boundaries obtained from tensor results. Finally, the locations of the structures were determined using tensor invariants.

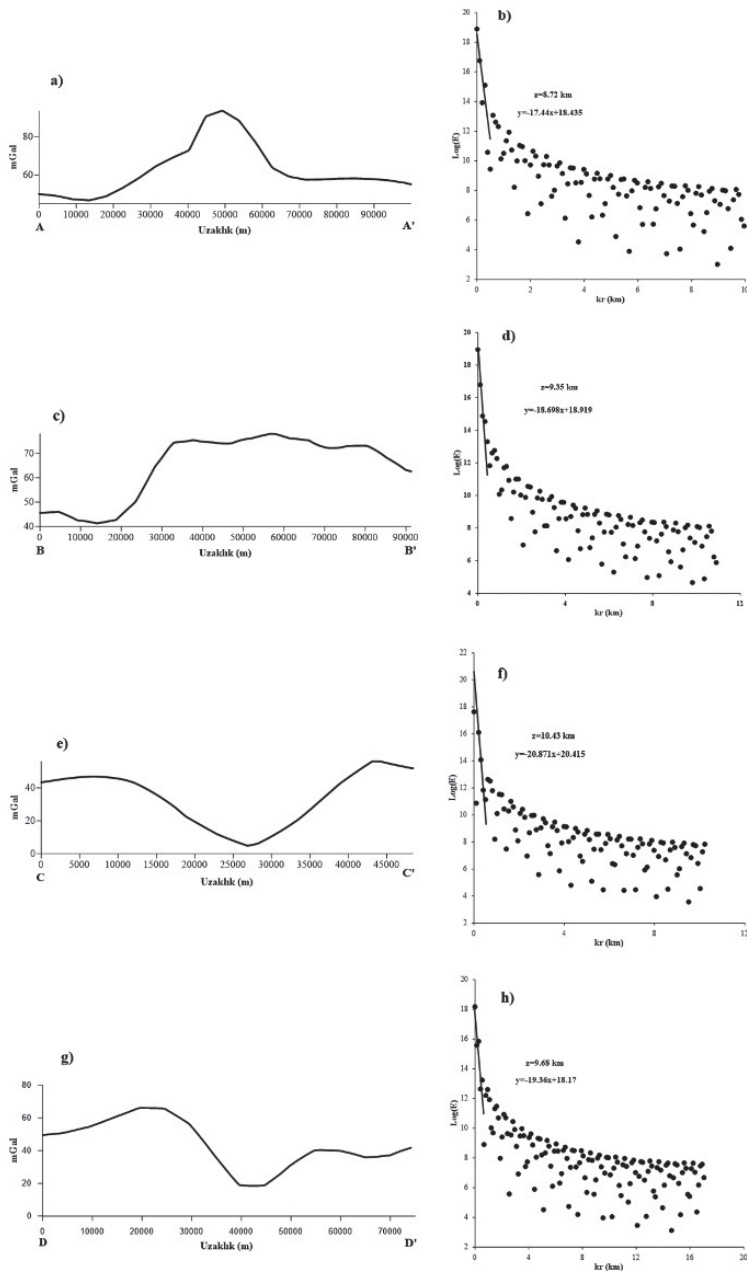


Figure 13. The profiles which were taken from Fig. 12 and the power spectrum results of profiles: (a) the anomaly of A-A' profile, (b) power spectrum result of A-A' profile, (c) the anomaly B-B' profile, (d) power spectrum result of B-B' profile, (e) the anomaly of C-C' profile, (f) power spectrum result of C-C' profile, (g) the anomaly of D-D' profile and (h) power spectrum result of D-D' profile.

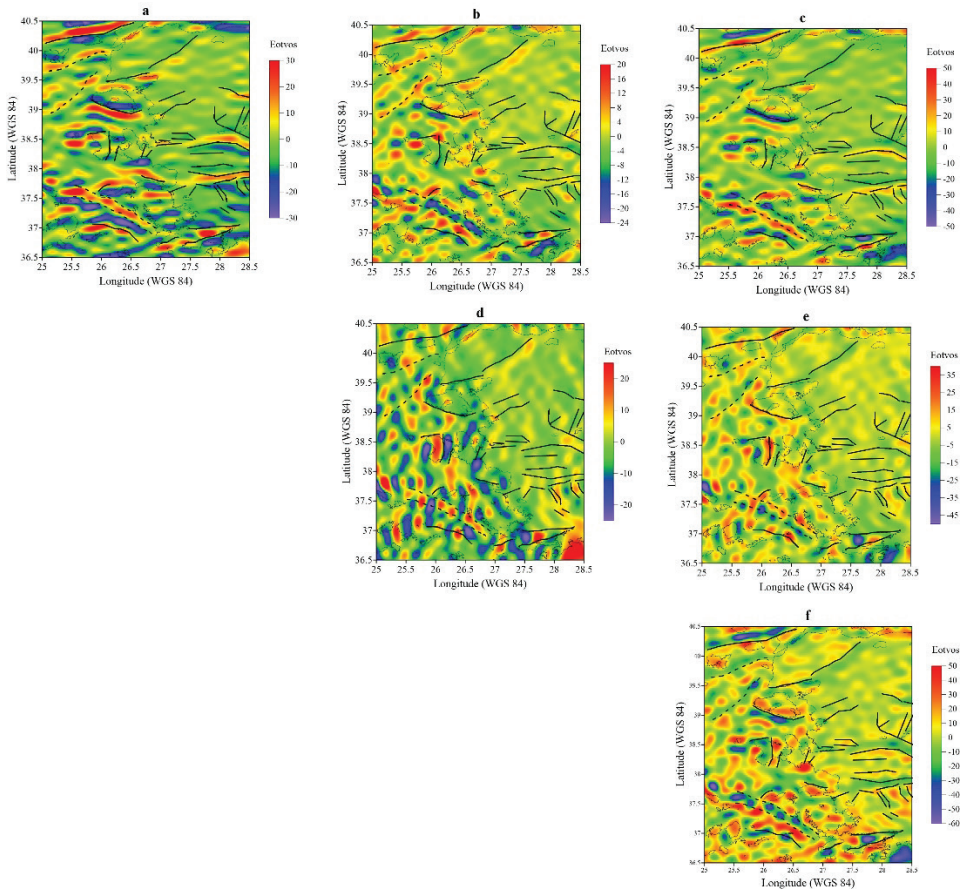


Figure 14. The results of disturbing tensors in the local North-oriented reference frame: (a) T_{xx} , (b) T_{xy} , (c) T_{xz} , (d) T_{yy} , (e) T_{yz} and (f) T_{zz} (solid black lines represent the active fault systems, light black line shows the coastline and dashed lines show the possible faults that are given in this study).

In the field study, first of all, the average depth was determined by using the logarithmic power spectrum method by taking the sections from the Bouguer gravity disturbances map (Fig. 12) in which three discontinuities are located. As a result of the power spectrum of the A-A' section, which was taken from Sigacik Gulf, an average depth of 8.72 km was obtained (Figs. 13a and 13b). Tiryakioğlu et al. (2018) obtained dipping normal type fault segment extending a depth down to ~ 9.5 km from co-slip results of Bodrum-Kos earthquake (Mw 6.6). In this study, an average depth of 9.35 km was obtained by the application of the power spectrum to section B-B' (Figs. 13c and 13d). Saltogianni et al. (2015) suggested right-lateral strike-slip fault at a depth of 11 km from seismic inversion of Samothraki-Gökçeada earthquake (Mw 6.9). Also, 10.43 km mean depth was obtained from

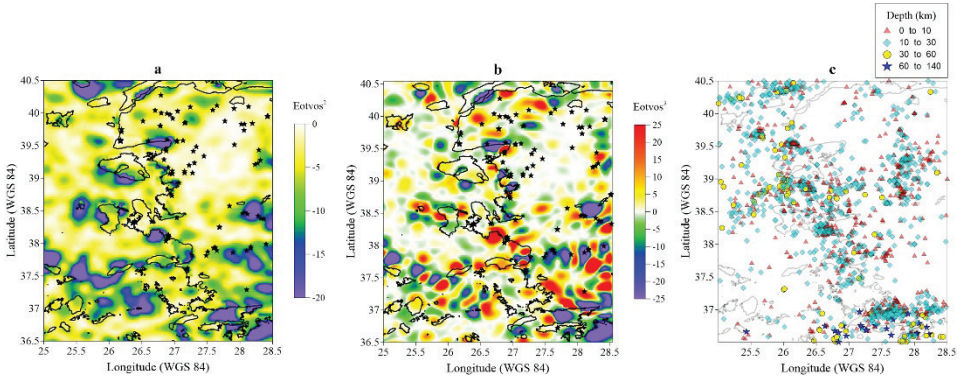


Figure 15. The results of I1 and I2 invariants and earthquake focal depth distribution ($M_w \geq 3.5$) between 1980 to 2018 of the study area (earthquake data was taken from <https://deprem.afad.gov.tr/ddakatalogu>): (a) the I1 invariant, (b) the I2 invariant and (c) earthquake distribution (black stars indicate the location of known geothermal hot spots in figures (a) and (b) from Tapirdamaz (2011)).

the power spectrum result of C-C' profile (Figs. 13e and 13f). Earthquakes which were bigger than 6.2 Mw occurred at approximately 10 km depth in the Midilli fault (Sozbilir et al., 2017). Finally, an averaged depth of 9.68 km value was obtained from power spectrum result of D-D' section (Figs. 13g and 13h).

When the tensor results are examined, it is seen that the T_{xx} , T_{xy} and T_{xz} components better represent the discontinuities than the T_{yy} and T_{yz} components (Figs. 14a to 14e). In addition, lateral discontinuities were observed as a result of the T_{zz} tensor which was the most successful to determine the boundaries (Fig. 14f). When the tensor results are examined, it can be said that the general discontinuities in the region are lateral and vertical continuity. When the GPS orientation results of Barka and Reilinger (1997) study are examined, it is thought that the fault that is at the south of the faults given by the dashed lines between the latitudes 39° – 40° may have come to the present situation via breaking from fault in the land. The discontinuity given by the dashed lines on the further north is particularly noticeable in the T_{xx} and T_{zz} tensors. Finally, the fault zone suggested by dashed lines in the south-west of the region is clearly in T_{xx} , T_{xy} , T_{xz} and T_{zz} tensors.

Local geothermal hot spots and distributions of earthquake focal depths for the study area were shown in Fig. 15. The regions where include the lowest amplitudes in the I1 invariant are related to the locations where the Seferihisar (2005), Gökçeada (2014), Midilli (2017) and Gökova (2017) earthquakes occurred. In addition, earthquake intensity was located as shown in Fig. 15c. The structure of a possible discontinuity between the 37° – 37.5° latitudes in Fig. 12 was observed in both I1 and I2 invariants (Figs. 15a and 15b). Also, the geothermal hot spot locations are a good agreement in the positive to negative anomaly borders of I2 invariant result and mostly minimum anomaly borders of I1 invariant re-

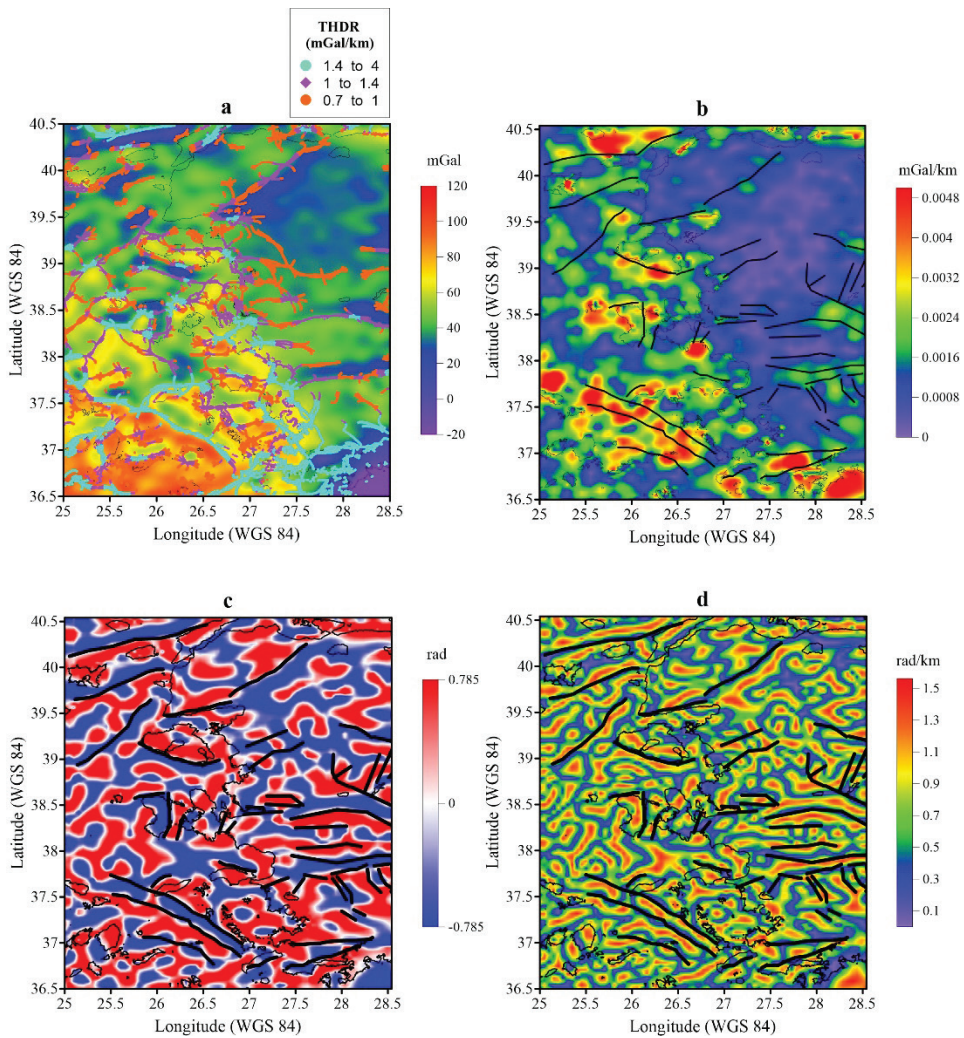


Figure 16. Boundary analysis results: (a) *THDR* result was overlaid on Bouguer gravity disturbance map, (b) the result of AS, (c) the result of tilt angle and (d) the result of theta map.

sult. This discontinuity has mostly low-amplitude gravity anomaly as shown in Fig. 12 and the area is not related to high seismicity as shown in Fig. 15c, indicating low-density content and possibly high heat flux.

When the boundary analysis results are examined, it was observed that the known discontinuities in the region are compatible with the *THDR* result (Fig. 16a). As a result of AS, high anomaly values were obtained in regions where discontinuities exist (Fig. 16b). Locations where the tilt angle values of 0 in the results give the boundary structures. When the results are examined, known

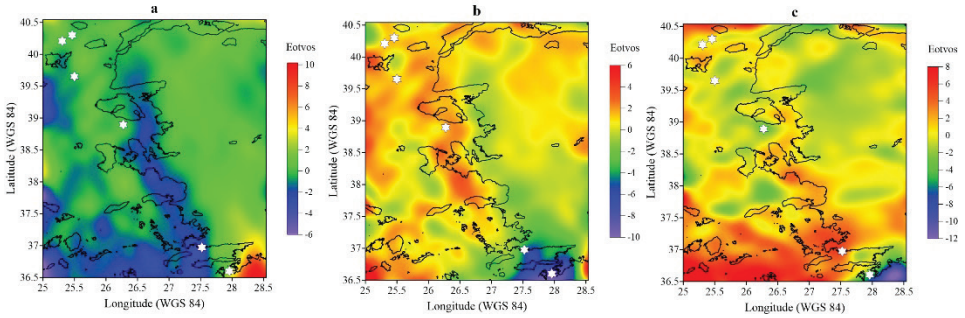


Figure 17. The upward continued (20 km) results of (a) T_{yy} , (b) T_{yz} and (c) T_{zz} components (white stars represent the big earthquakes that occurred in the last three year).

discontinuity boundaries were observed clearly in tilt angle and theta map results (Figs. 16c and 16d). Especially with the distribution of seismicity in Fig. 15c and Fig. 16b are very compatible. The location where seismicity was not observed is the discontinuity zone defined between 37° – 37.5° latitudes.

When the results of the upward extension are examined, it is seen that the deeper structure is in the North-South orientation but the shallow tectonic elements are in the East-West orientation (Fig. 17). In particular, it is thought that the Western Anatolian Transfer Zone (WATZ) is the cause of the North-South direction anomalies in the results of the upward extension of the T_{yy} tensor (Gessner, 2013; Doğru et al., 2017).

5. Conclusions

In recent years, Western Anatolian and the Aegean Sea regions have offered active seismicity so the locations and depths of the tectonic structures that create this seismic activity were investigated in this study. The tensors, invariants, power spectrum and boundary analysis methods were applied to the both theoretical and case study. To determine the extensions of shallow tectonic structures, gravity disturbance data which better reflect the properties of surface tectonic elements were used. The depths of known faults were obtained using the logarithmic power spectrum and the results were compared with previous studies in the literature. In addition, the boundaries of structures were obtained using invariants, tensors and boundary analysis methods like tilt angle, total horizontal derivative, analytic signal and theta map. As a result of the study, known tectonic elements of Western Anatolia and the Aegean Sea were determined and also the extensions and boundaries of new discontinuities contributing to literature were determined and interpreted.

Acknowledgements – This study is a part of the PhD thesis of Fikret DOĞRU at the Institute of Natural and Applied Sciences in DEU, Izmir, Turkey. We would like to thank Prof. Dr. Abdullah Ates for his contribution with personal communications. This study is funded by Dokuz Eylül University No 2018.KB.FEN.013 Scientific Research Project.

References

- Alptekin, Ö. (1973): *Focal mechanisms of earthquakes in western Turkey and their tectonic implications*, PhD Thesis, New Mexico Institute of Mining and Technology.
- Arisoy, M. Ö. and Dikmen, Ü. (2013): Geliştirilmiş eğim açısı toplam yatay türevi ile manyetik kaynakların sınırlarının belirlenmesi, *Yerbilimleri Dergisi*, **34**, 141–168.
- Barka, A. and Reilinger, R. (1997): Active tectonics of the Eastern Mediterranean region: Deduced from GPS, neotectonic and seismicity data, *Ann. Geophys.-Italy*, **40**, 587–610, DOI: 10.4401/ag-3892.
- Beiki, M. and Pedersen, L. B. (2010): Eigenvector analysis of gravity gradient tensor to locate geologic bodies, *Geophysics*, **75**, 137–149, DOI: 10.1190/1.3484098.
- Bozkurt E. (2001): Neotectonics of Turkey – a synthesis, *Geodin. Acta*, **14**, 3–30, DOI: 10.1080/09853111.2001.11432432.
- Bucha, B. and Janák, J. (2013): A MATLAB-based graphical user interface program for computing functionals of the geopotential up to ultra-high degrees and orders, *Comput. Geosci.-UK*, **56**, 186–196, DOI: 10.1016/j.cageo.2013.03.012.
- Çırmık, A. and Pamukçu, O. (2017): Clarifying the interplate main tectonic elements of Western Anatolia, Turkey by using GNSS velocities and Bouguer gravity anomalies, *J. Asian Earth Sci.*, **148**, 294–304, DOI: 10.1016/j.jseae.2017.09.001.
- Çırmık, A., Pamukçu, O., Gönenc, T., Kahveci, M., Şalk, M. and Herring, T. (2017): Examination of the kinematic structures in İzmir (Western Anatolia) with repeated GPS observations (2009, 2010 and 2011), *J. Afr. Earth Sci.*, **126**, 1–12, DOI: 10.1016/j.jafrearsci.2016.11.020.
- Cordell, L. and Grauch, V. J. S. (1985): Mapping basement magnetization zones from aeromagnetic data in The San Juan Basin, New Mexico, in: *The utility of regional gravity and magnetic anomaly maps: Society exploration geophysics*, Tulsa, Oklahoma, USA, 181–197, DOI: 10.1190/1.1826915.
- Dewey, J. F. (1988): Extensional collapse of orogens, *Tectonics*, **7**, 1123–1139, DOI: 10.1029/TC007i006p01123.
- Dewey, J. F. and Şengör, A. M. C. (1979): Aegean and surrounding regions: complex multiplate and continuum tectonics in a convergent zone, *Bull. Geol. Soc. Am.*, **90**, 84–92, DOI: 10.1130/0016-7606(1979)90<84:AASRCM>2.0.CO;2.
- Dickinson, J. L., Brewster, J. R., Robinson, J. W. and Murphy, C. A. (2009): Imaging techniques for full tensor gravity gradiometry data, in: *11th SAGA Biennial Technical Meeting and Exhibition*, 84–86.
- Doğru, F., Pamukçu, O. and Ozsoz, I. (2017): Application of tilt angle method to the Bouguer gravity data of Western Anatolia, *Bull. Mineral Res. Expl.*, **155**, 213–222, DOI: 10.19111/bulletinofmre.305177.
- Doğru, F., Pamukçu, O., Gönenc, T. and Yildiz, H. (2018): Lithospheric structure of western Anatolia and the Aegean Sea using GOCE-based gravity field models, *B. Geofis. Teor. Appl.*, **59**, 135–160, DOI: 10.4430/bgta0231.
- Dransfield, M. and Milkereit, B. (2007): Airborne gravity gradiometry in the search for mineral deposits, in *Proceedings of Exploration 07: Fifth Decennial International Conference on Mineral Exploration*, edited by Milkereit, B., **7**, 341–354.
- Gessner, K., Gallardo, L. A., Markwitz, V., Ring, U. and Thomson, S. N. (2013): What caused the denudation of the Mendere Massif: Review of crustal evolution, lithosphere structure, and dynamic topography in southwest Turkey, *Gondwana Res.*, **24**, 243–274, DOI: 10.1016/j.gr.2013.01.005.
- Gönenc, T. and Akgün, M. (2012): Structure of the Hellenic subduction zone from gravity gradient functions and seismicology, *Pure Appl. Geophys.*, **169**, 1231–1255, DOI: 10.1007/s00024-011-0391-2.
- Grombein, T., Luo, X., Seitz, K. and Heck, B. (2014): A wavelet-based assessment of topographic-isostatic reductions for GOCE gravity gradients, *Surv. Geophys.*, **35**, 959–982, DOI: 10.1007/s10712-014-9283-1.
- <https://depem.afad.gov.tr/ddakatalogu>
- Kahveci, M., Çırmık, A., Doğru, F., Pamukçu, O. and Gönenc, T. (2019): Subdividing the tectonic elements of Aegean and Eastern Mediterranean with gravity and GPS data, *Acta Geophys.*, **67**, 491–500, DOI: 10.1007/s11600-019-00270-w.

- Klokočník, J., Kostecký, J., Kalvoda, J., Eppelbaum, L. V. and Bezděk, A. (2014): Gravity disturbances, Marussi tensor, invariants and other functions of the geopotential represented by EGM 2008, *J. Earth Sci. Res.*, **2**(3), 88–101, DOI: [10.18005/JESR0203003](https://doi.org/10.18005/JESR0203003).
- Le Pichon, X. and Angelier, J. (1979): The hellenic arc and trench system: A key to the evolution of the eastern Mediterranean area, *Tectonophysics*, **60**, 1–42 DOI: [10.1016/0040-1951\(79\)90131-8](https://doi.org/10.1016/0040-1951(79)90131-8).
- Malalıcı, B. C., Pamukçu O., Çırmık, A. and Dindar, H. (2019): Deformation analysis of East Mediterranean with using SSPX software, *DEUFMD*, **21**(61), 235–246, DOI: [10.21205/deufmd.2019216123](https://doi.org/10.21205/deufmd.2019216123).
- Makris, J. and Stobbe, C. (1984): Physical properties and state of the crust and upper mantle of the eastern Mediterranean Sea deduced from geophysical data, *Marine Geology*, **55**, 347–363, DOI: [10.1016/0025-3227\(84\)90076-8](https://doi.org/10.1016/0025-3227(84)90076-8).
- Mataragio, J. and Kieley, J. (2009): Use of full tensor gravity invariants in detection of intrusion-hosted sulphide mineralization: Implications for emplacement mechanisms, in: *11th International Congress of the Brazilian Geophysical Society*, 723–726, DOI: [10.1190/sbgf2009-159](https://doi.org/10.1190/sbgf2009-159).
- McClusky, S., Balassanian, S., Barka, A., Demir, C., Ergintav, S., Georgiev, I., Gurkan, O., Hamburger, M., Hurst, K., Kahle, H., Kasten, K., Kekelidze, G., King, R. W., Kotzev, V., Lenk, O., Mahmoud, S., Mishin, A., Nadariya, M., Ouzoumis, A., Paradissis, D., Peter, Y., Prilepin, M., Reilinger, R., Sanli, I., Seeger, H., Tealeb, A., Toksöz, M. N. and Veis, G. (2000): GPS constraints on plate kinematics and dynamics in the eastern Mediterranean and Caucasus, *J. Geophys. Res. – Sol. Ea.*, **105**, 5695–5719.
- McKenzie, D. (1972): Active tectonics of the Mediterranean region, *Geophys. J. Int.*, **30**, 109–185, DOI: [10.1111/j.1365-246X.1972.tb02351.x](https://doi.org/10.1111/j.1365-246X.1972.tb02351.x).
- Meulenkamp, J. E., Wortel, W. J. R., Van Wamel, W. A., Spakman, W. and Hoogerduyn, S. E. (1988): Hellenic subduction zone and geodynamic evolution of Crete since the late Middle Miocene, *Tectonophysics*, **146**, 203–205, DOI: [10.1016/0040-1951\(88\)90091-1](https://doi.org/10.1016/0040-1951(88)90091-1).
- Miller, H. G. and Singh, V. (1994): Potential field tilt – a new concept for location of potential field sources, *J. Appl. Geophys.*, **32**, 213–217, DOI: [10.1016/0926-9851\(94\)90022-1](https://doi.org/10.1016/0926-9851(94)90022-1).
- Murphy, C. A. and Brewster, J. (2007): Target delineation using full tensor gravity gradiometry data, *ASEG Extended Abstracts*, **2007**, 1–3, DOI: [10.1071/ASEG2007ab096](https://doi.org/10.1071/ASEG2007ab096).
- Murphy, C. A. and Dickinson, J. L. (2009): Exploring exploration play models with FTG gravity data, in: *11th SAGA Biennial Technical Meeting and Exhibition*, Swaziland, 16–18 September 2009, 89–91.
- Murphy, C. A. and Dickinson, J. L. (2010): Geological mapping and targeting using invariant tensor analysis on full tensor gravity data, in: *EGM 2010 International Workshop “Adding new value to electromagnetic, gravity and magnetic methods for exploration”*, Capri, Italy, 11–14 April 2010, 5 pp.
- Oruç, B. (2010): Depth estimation of simple causative sources from gravity gradient tensor invariants and vertical component, *Pure Appl. Geophys.*, **167**, 1259–1272, DOI: [10.1007/s00024-009-0021-4](https://doi.org/10.1007/s00024-009-0021-4).
- Oruç, B., Sertçelik, I., Kafadar, Ö. and Selim, H. H. (2013): Structural interpretation of the Erzurum Basin, eastern Turkey, using curvature gravity gradient tensor and gravity inversion of basement relief, *J. Appl. Geophys.*, **88**, 105–113, DOI: [10.1016/j.jappgeo.2012.10.006](https://doi.org/10.1016/j.jappgeo.2012.10.006).
- Pavlis, N. K., Holmes, S. A., Kenyon, S. C. and Factor, J. K. (2008): An earth gravitational model to degree 2160: EGM2008, EGU General Assembly, Vienna, Austria, 13–18 April, 4–2.
- Pawlowski, R. S. (1994): Green’s equivalent-layer concept in gravity band-pass filter design, *Geophysics*, **59**, 69–76, DOI: [10.1190/1.1443535](https://doi.org/10.1190/1.1443535).
- Pawlowski, R. S. and Hansen, R. O. (1990): Gravity anomaly separation by Wiener filtering, *Geophysics*, **55**, 539, DOI: [10.1190/1.1442865](https://doi.org/10.1190/1.1442865).
- Pedersen, L. B. and Rasmussen, T. M. (1990): The gradient tensor of potential field anomalies: Some implications on data collection and data processing of maps, *Geophysics*, **55**, 1558–1566, DOI: [10.1190/1.1442807](https://doi.org/10.1190/1.1442807).
- Roest, W. R., Verhoef, J. and Pilkington, M. (1992): Magnetic interpretation using the 3-D analytic signal, *Geophysics*, **57**, 116–125, DOI: [10.1190/1.1443174](https://doi.org/10.1190/1.1443174).

- Routh, P. S., Jorgensen, G. J. and Kisabeth, J. L. (2001): Base of the salt imaging using gravity and tensor gravity data, in: *SEG Technical Program Expanded Abstracts 2001*, Society of Exploration Geophysicists Annual Meeting, San Antonio, 1482–1484.
- Saltogian, V., Giannou, M., Taymaz, T., Yolsal-Çevikbilen, S. and Stiros, S. (2015): Fault slip source models for the 2014 *M_w* 6.9 Samothraki-Gökçeada earthquake (North Aegean trough) combining geodetic and seismological observations, *J. Geophys. Res.–Sol. Ea.*, **120**, 8610–8622, DOI: 10.1002/2015JB012052.
- Şengör A. M. C. (1979): The north Anatolian transform fault: Its age, offset and tectonic significance, *J. Geol. Soc. London*, **136**, 269–282, DOI: 10.1144/gsjgs.136.3.0269.
- Şengör, A. M. C., Görür, N. and Şaroğlu, F. (1985): Strike-slip faulting and related basin formation in zones of tectonic escape: Turkey as a case study, *Strike-Slip Deformation, Basin Formation, and Sedimentation*, SEPM Special Publication, edited by Biddle, K. T. and Christie-Blick, N. **37**, 227–264, DOI: 10.2110/pec.85.37.0211.
- Şengör A. M. C. (1987): Cross-faults and differential stretching of hanging walls in regions of low-angle normal faulting: examples from western Turkey, *Geol. Soc. London Spec. Pub.*, **28**, 575–589, DOI: 10.1144/GSL.SP.1987.028.01.38.
- Seyitoğlu, G. and Scott, B. (1991): Late Cenozoic crustal extension and basin formation in west Turkey, *Geol. Mag.*, **128**, 155–166, DOI: 10.1017/S0016756800018343.
- Sözbilir, H., Sümer, O., Uzel, B., Eski, S. and Softa, M. (2017): 12 haziran 2017 midilli depremi (Karaburun Acıkları) ve bölgenin depremselliği, *Technical Report*, DOI: 10.13140/RG.2.2.19984.20481.
- Spector, A. and Grant, F. (1970): Statistical models for interpreting aeromagnetic data, *Geophysics*, **35**, 293–302, DOI: 10.1190/1.1440092.
- Tapırdamaz, M. C. (2011): Yerbilimleri veri kataloğu, *Active Tectonics Research Group (ATAG 15), Proceeding Books*, **66**, Çukurova University, Adana.
- Tiryakioğlu, İ., Aktuğ, B., Yiğit, C. Ö., Yavaşoğlu, H. H., Sözbilir, H., Özkaymak, Ç., Poyraz, F., Taneli, E., Bulut, F., Dođru, A. and Özener, H. (2018): Slip distribution and source parameters of the 20 July 2017 Bodrum-Kos earthquake (*M_w*6.6) from GPS observations, *Geodin. Acta*, **30**, 1–14, DOI: 10.1080/09853111.2017.1408264.
- Wijns, C., Perez, C. and Kowalczyk, P. (2005): Theta map: Edge detection in magnetic data, *Geophysics*, **70**, L39-L43, DOI: 10.1190/1.1988184.
- Zhang, C., Mushayandebvu, M. F., Reid, A. B., Fairhead, J. D. and Odegard, M. E. (2000): Euler deconvolution of gravity tensor gradient data, *Geophysics*, **65**, 512–520, DOI: 10.1190/1.1444745.
- Zhdanov, M. S., Ellis, R. and Mukherjee, S. (2004): Three-dimensional regularized focusing inversion of gravity gradient tensor component data, *Geophysics*, **69**, 925–937, DOI: 10.1190/1.17778236.
- Zhou, W. (2016): Depth estimation method based on the ratio of gravity and full tensor gradient invariant, *Pure Appl. Geophys.*, **173**, 499–508, DOI: 10.1007/s00024-015-1117-7.
- Zuo, B. and Hu, X. (2015): Edge detection of gravity field using eigenvalue analysis of gravity gradient tensor, *J. Appl. Geophys.*, **114**, 263–270, DOI: 10.1016/j.jappgeo.2015.01.013.
- Zuo, B., Kass, M. A., Hu, X. and Geng, M. (2017): Full-tensor gravity gradient eigenvector analysis for locating complex geological source positions, *Nonlin. Processes Geophys. Discuss.*, DOI: 10.5194/npg-2016-75.

SAŽETAK

Analiza poremećaja ubrzanja sile teže graničnih struktura na području Egejskog mora i Zapadne Anatolije

Fikret Dođru i Oya Pamukçu

Zapadna Anatolija je oblikovana u smjeru sjever-jug zahvaljujući ekstenzivnom tektonskom trendu i zapadno-istočnim uzdizanjima, grebenima I aktivnim rasjedima kao posljedicom kolizije Afričke, Arapske i Euroazijske ploče. Granice tektonskog područja

Egejskog mora ograničene su između istočne Grčke, zapadne Anatolije i Helenske subdukcijske zone na jugu Krete. Za procjenu tih tektonskih elemenata korišteni su podaci o poremećaju ubrzanja sile teže na području Egejskog mora i Zapadne Anatolije. Smatra se da podaci o poremećaju ubrzanja sile teže odražavaju tektonske elemente i diskontinuitete bolje nego anomalija ubrzanja sile teže zbog računanja razlike između ubrzanja sile teže i normalnog ubrzanja sile teže na istoj točki, tako da su izračunati tenzori i invarijante na promatranom području i metoda spektra snage je primijenjena na podatke poremećaja ubrzanja sile teže kako bi se usporedili diskontinuiteti dobiveni iz tenzora. Te su metode najprije ispitane na teoretskim podacima. U okviru teorijske studije uzeti su u obzir jedan samostalni model i tri modela tijela. Prilikom interpretacije rezultata, uočeno je da T_{zz} tenzorska komponenta daje vrlo jasne informacije o lokaciji strukture. Isto tako, kada se ispituju T_{xx} , T_{yy} komponente i nepromjenjivi rezultati, uspješno su dobivene vertikalne i horizontalne granice. Također, srednje dubine tih struktura određene su metodom spektra snage. U stupnju primjene slučaja ispitani su podaci poremećaja ubrzanja sile teže generirani iz Zemljinog gravitacijskog modela EGM na području istočnog Egejskog mora i zapadne Anatolije. Najprije su izračunati tenzor i invarijante poremećaja ubrzanja sile teže. Identificirani su novi mogući diskontinuiteti u tenzorima, a neki od dobivenih diskontinuiteta razjašnjeni su u prethodnim raspravama. Također, prosječne dubine mogućih struktura izračunate su metodom spektra snage na četiri profila iz podataka o poremećaju ubrzanja sile teže. Ove dubinske vrijednosti su u skladu s dubinskim vrijednostima strukturnih diskontinuiteta dobivenih iz prethodnih studija. Naposljetku, kontinuirana prema gore primijenjen je na tenzore T_{yy} , T_{yz} i T_{zz} do 20 km. Vrijednosti pozitivnih anomalija u T_{yz} i T_{zz} komponentama i negativne vrijednosti anomalija u T_{yy} komponenti u skladu su sa transfer zonom Zapadne Anatolije. Strukturne razlike između istočnog i zapadnog dijela Zapadne Anatolije značajne su u daljnjim rezultatima tenzora. Također, pozitivne i negativne anomalije su značajne u područjima gdje su se dogodili veliki potresi u posljednje 3 godine u T_{yz} invarijantama.

Ključne riječi: poremećaj ubrzanja sile teže, Egejsko more, zapadna Anatolija, tenzor, invarijanta

Corresponding author's address: Fikret Doğru, Department of Geophysical Engineering, Oltu Earth Sciences Faculty, Ataturk University, Oltu, Erzurum, Turkey; e-mail: fikretdogru@atauni.edu.tr



This work is licensed under a Creative Commons Attribution-NonCommercial 4.0 International License.